



Arzilli, F., La Spina, G., Burton, M., Polacci, M., Le Gall, N., Hartley, M., Di Genova, D., Cai, B., Vo, N., Bamber, E., Nonni, S., Atwood, R., Llewellyn, E., Brooker, R., Mader, H., & Lee, P. (2019). Magma fragmentation in highly explosive basaltic eruptions induced by rapid crystallisation. *Nature Geoscience*, 12, 1023–1028.  
<https://doi.org/10.1038/s41561-019-0468-6>

Peer reviewed version

Link to published version (if available):  
[10.1038/s41561-019-0468-6](https://doi.org/10.1038/s41561-019-0468-6)

[Link to publication record in Explore Bristol Research](#)  
PDF-document

This is the author accepted manuscript (AAM). The final published version (version of record) is available online via Springer Nature at <https://www.nature.com/articles/s41561-019-0468-6#article-info>. Please refer to any applicable terms of use of the publisher.

## University of Bristol - Explore Bristol Research

### General rights

This document is made available in accordance with publisher policies. Please cite only the published version using the reference above. Full terms of use are available:  
<http://www.bristol.ac.uk/red/research-policy/pure/user-guides/ebr-terms/>

1 Accepted version before minor changes;

2 **Magma fragmentation in highly explosive basaltic eruptions induced by rapid crystallisation**

3

4 Fabio Arzilli<sup>1</sup>, Giuseppe La Spina<sup>1</sup>, Mike R. Burton<sup>1</sup>, Margherita Polacci<sup>1</sup>, Nolwenn Le Gall<sup>2</sup>,  
5 Margaret E. Hartley<sup>1</sup>, Danilo Di Genova<sup>3</sup>, Biao Cai<sup>4</sup>, Nghia T. Vo<sup>5</sup>, Emily C. Bamber<sup>1</sup>, Sara  
6 Nonni<sup>5</sup>, Robert Atwood<sup>5</sup>, Ed W. Llewellyn<sup>6</sup>, Richard A. Brooker<sup>7</sup>, Heidy Mader<sup>7</sup> and Peter D. Lee<sup>2</sup>

7

8 <sup>1</sup>School of Earth and Environmental Sciences, University of Manchester, Manchester M139PL, UK

9 <sup>2</sup>Department of Mechanical Engineering, University College London, London, UK

10 <sup>3</sup>Institute of Non-Metallic Materials, Clausthal University of Technology, Zehntner Str. 2a, 38678  
11 Clausthal-Zellerfeld, Germany

12 <sup>4</sup> School of Metallurgy and Materials, University of Birmingham, Birmingham B15 2TT, UK

13 <sup>5</sup>Diamond Light Source, Harwell Science and Innovation Campus, Didcot OX11 0DE, UK

14 <sup>6</sup>Department of Earth Sciences, Durham University, Durham DH1 3LE, UK

15 <sup>7</sup>School of Earth Sciences, University of Bristol, Bristol BS8 1RJ, UK

16

17

18 \*Corresponding author: Dr. Fabio Arzilli

19 Corresponding author present affiliation: School of Earth and Environmental Sciences, The  
20 University of Manchester, Oxford Road, Manchester, M13 9PL, UK

21 E-mail address: fabio.arzilli@manchester.ac.uk

22 Phone: +393298429732; +447904104670

23

24

25 Basaltic eruptions are the most common form of volcanism on Earth and planetary bodies.  
26 The low viscosity of basaltic magmas inhibits fragmentation, favouring effusive and lava-  
27 fountaining activity, yet highly explosive, hazardous basaltic eruptions do occur. The  
28 processes that promote fragmentation of basaltic magma remain unclear, and are subject to  
29 debate. Here, we use a numerical conduit model to show that rapid ascent of magma during  
30 explosive eruption produces large undercooling. Novel *in situ* experiments reveal that  
31 undercooling drives exceptionally rapid (~minutes) crystallisation, inducing a step-change in  
32 viscosity that triggers magma fragmentation. Experimentally-produced textures are  
33 consistent with products of basaltic Plinian eruptions. We apply the numerical model to  
34 investigate basaltic magma fragmentation over a wide parameter space and find that all  
35 basaltic volcanoes have the potential to produce highly explosive eruptions. The critical  
36 requirements are initial magma temperatures lower than 1100 °C, in order to reach a syn-  
37 eruptive crystal content of > 30 vol.%, and thus a magma viscosity  $\geq 10^5$  Pa s, which our  
38 results suggest is the minimum viscosity required for the fragmentation of fast ascending  
39 basaltic magmas. Our study provides both a demonstration and explanation of the processes  
40 that drive basaltic Plinian eruptions, revealing how typically effusive basaltic volcanoes can  
41 produce unexpected highly explosive, and hazardous, eruptions.

42

Explosive eruptions are undoubtedly the most violent and catastrophic expression of volcanic activity<sup>1,2</sup>. Highly explosive Plinian eruptions can inject  $> 0.1 \text{ km}^3$  of pyroclastic material producing volcanic plumes that can reach up to 40 km in height, impacting both regional and global climate, and producing a significant threat to proximal populations<sup>3,4</sup>. Basaltic volcanoes are usually characterised by effusive and mild-explosive lava fountaining activity<sup>5</sup>, however, basaltic Plinian eruptions can occur<sup>6-11</sup>. The main process characterising highly explosive activity is magma fragmentation, which is the transition from ductile to brittle behaviour of molten magma<sup>1,2</sup>. For silicic magmas, fragmentation is attributed to high strain rates associated with acceleration of the bubbly mixture<sup>1,12-14</sup> or from the bubble overpressure associated with restricted bubble expansion<sup>14,15-18</sup>. The low viscosity of basaltic magmas, however, makes high strain rates, or the bubble overpressure necessary to trigger fragmentation difficult to achieve<sup>1,19</sup>.

Crystallisation during magma ascent may significantly increase magma viscosity, leading to fragmentation<sup>20</sup>. However, crystallisation in basaltic magmas has previously been thought to occur on timescales significantly longer than the time required for magma to ascend from a crustal storage chamber to the vent<sup>21</sup>, particularly in the case of highly explosive eruptions.

In volcanic conduits, the crystallisation kinetics of an ascending magma are driven by degassing and cooling<sup>22-23</sup>. Plagioclase and pyroxene crystallisation are sensitive indicators of magma dynamics in volcanic conduits<sup>21,24-27</sup> and their kinetically controlled abundance can rapidly change magma rheology<sup>28-29</sup>. Our understanding of crystallisation kinetics in magmas is underpinned by *ex situ* crystallisation quench experiments. Here we perform novel *in situ* experiments in order to visualize and quantify the evolution of rapid crystallisation in basaltic magmas, as with this approach it is possible to ascertain in real time when crystals start to form and how quickly magma crystallinity evolves.

A frequently used model to describe crystallisation as function of time is given by an exponential law<sup>21,23</sup>, where the rate of crystallisation is controlled by the characteristic time  $\tau^{(c)}$ . The characteristic time is a measure of how fast a process will approach the equilibrium<sup>21,30</sup>. The smaller

69  $\tau^{(c)}$ , the faster crystals reach their equilibrium abundance (see Methods section). La Spina et al. (ref.  
70 21) demonstrated that the time required to reach the equilibrium crystal fraction in basalts is  $\sim 4.6$   
71 times  $\tau^{(c)}$ . Furthermore, during mild lava-fountaining basaltic activity<sup>21</sup>,  $\tau^{(c)}$  is in the order of  
72 thousands seconds, resulting in a crystallisation time of  $\sim 2$  hours. Crystallisation rate increases with  
73 magma ascent rate, as cooling and decompression rates increase<sup>30-34</sup>. Therefore,  $\tau^{(c)}$  is smaller and  
74 the equilibrium crystal fraction will be reached faster. However, the characteristic times of crystal  
75 growth during fast magma ascent have not been quantified.

76 In order to quantify the characteristic times of plagioclase and pyroxene crystallisation during  
77 rapid ascent of basaltic magma, here we present the first *in situ* 4D (3D plus time) crystallisation  
78 kinetics experiments under fast cooling rates, using fast synchrotron X-ray microtomography. Our  
79 experiments provide the first estimation of the characteristic time for plagioclase and pyroxene  
80 crystallisation in trachybasaltic magmas during a rapid and continuous increase of undercooling,  
81 where  $\Delta T$  is defined as the difference between the highest temperature at which plagioclase and  
82 pyroxene is expected to crystallise and the temperature of the magma<sup>24-27</sup>.

83

#### 84 **Crystallisation experiments at high undercooling**

85 Crystallisation experiments were performed *in situ* at beamline I12-JEEP, Diamond Light  
86 Source, Harwell, UK, using a trachybasaltic glass (Supplementary Table 1) from the 2001 Etna  
87 eruption as the starting material (see Methods). We combined a bespoke high-temperature  
88 environmental cell<sup>35</sup> with fast synchrotron X-ray microtomography to image the evolution of  
89 crystallisation in real time<sup>36</sup> in two experiments. In the first part of the experiment, crystallisation  
90 was induced by decreasing temperature from 1250 °C to either 1170 °C or 1150 °C at 0.4 °C s<sup>-1</sup> at  
91 ambient pressure with a dwell time at the final temperature of 4 h<sup>36</sup> (Supplementary Fig. 1). During  
92 these 4 h, blocky and prismatic clinopyroxene and oxide crystals were able to grow<sup>36</sup> (Fig. 1 and  
93 Supplementary Figs. 2 and 3), and the residual melt evolved to a basaltic trachyandesitic  
94 composition (Supplementary Table 1; Supplementary Figs. 2 and 3). After 4 h at sub-liquidus

95 conditions (1170 °C and 1150 °C), the system was perturbed through a rapid cooling rate of 0.4 °C  
96 s<sup>-1</sup>, inducing a sudden and continuous increase of undercooling ( $\Delta T$ ). This produced a rapid  
97 crystallisation event from the residual melt (Fig. 1; Supplementary Figs. 2 and 3). Our results show  
98 that skeletal plagioclase crystals grew during this final stage of rapid cooling, specifically between  
99 1112 and 1073 °C after a dwell time of 4 hours at 1150 °C (Fig. 1) and between 1131 and 1053 °C  
100 after a dwell time of 4 hours at 1170 °C (Supplementary Fig. 3a,b,c). Plagioclase crystals grew to  
101 equilibrium abundance in ~100 seconds (Fig.1), i.e. between two 3D scans. Following this initial  
102 burst of rapid plagioclase growth, dendritic clinopyroxene crystals began to nucleate  
103 heterogeneously on plagioclase and grew to their final size in the following 180 seconds (Fig. 1b,c;  
104 Supplementary Figs. 2b,c, 3d,e, 4 and 5).

105 The large  $\Delta T$  reached in a relatively short time during our *in situ* 4D crystallisation experiments  
106 generated distinctive skeletal plagioclase crystals with swallow-tail morphology and dendritic  
107 pyroxene (Fig. 2a-c), similar to the skeletal plagioclase and dendritic pyroxene crystals observed in  
108 the products of explosive basaltic Plinian eruptions<sup>7-11,37,38</sup>, such as Etna 122 B.C.<sup>7,8,37,38</sup> (Fig. 2d).  
109 Heterogeneous nucleation of dendritic pyroxene on skeletal plagioclase (Fig. 1b) is observed to  
110 occur in ~180 s during our 4D experiments. These distinctive textures are also reported in products  
111 of the Fontana Lapilli (Nicaragua)<sup>11,37,38</sup> and 1886 Tarawera (New Zealand) eruptions<sup>7,9,10</sup>.  
112 Therefore, all the studied examples of basaltic Plinian deposits show features that are consistent  
113 with the textures produced in our experiments. Furthermore, the signature skeletal and dendritic  
114 pyroxene is also observed in sub-Plinian eruption (Yufune 2) products of Mt. Fuji (Japan)<sup>39</sup>.

115 Skeletal plagioclase crystallisation occurred at  $\Delta T$  between 60 and 140 °C with a growth rate of  
116  $3 \times 10^{-5}$  cm s<sup>-1</sup> (mm h<sup>-1</sup>) (Supplementary Table 2), whilst dendritic pyroxene crystallised at  $\Delta T$   
117 between 60 and 175 °C with a growth rate of  $2 \times 10^{-5}$  cm s<sup>-1</sup> (mm h<sup>-1</sup>) (Supplementary Table 2). This  
118 indicates that a rapid increase of  $\Delta T$  (>60 °C) induces fast crystallisation. As the equilibrium  
119 pyroxene crystal content is achieved within ~180 s, we can infer that the pyroxene characteristic  
120 time under large  $\Delta T$  is < 40 s. For plagioclase, where the equilibrium crystal content is achieved

121 within 90 s the characteristic time is  $< 20$  s. These are about two orders of magnitude less than the  
122 characteristic time found by La Spina et al. (ref. 21) for effusive and mild lava fountaining activity  
123 at Etna (Italy), Stromboli (Italy) and Kilauea (Hawaii), which involved much smaller  $\Delta T$  (30-60  
124  $^{\circ}\text{C}$ )<sup>21</sup> and magma ascent rates of  $\sim 3 \text{ m s}^{-1}$ .

125 *Ex situ* experiments were also performed using a TZM cold seal pressure vessel apparatus, in  
126 order to investigate whether fast crystallisation also occurs in a hydrous trachybasaltic melt during  
127 rapid and continuous cooling and decompression (see Methods), simulating fast magma ascent in  
128 the conduit. The experimental approach consisted of holding the sample for 30 minutes at 75 MPa  
129 and 1070  $^{\circ}\text{C}$  before the sample was decompressed and the temperature decreased. After 30 minutes  
130 pressure and temperature were decreased continuously for 300 s at  $0.2 \text{ MPa s}^{-1}$  and  $0.2 \text{ }^{\circ}\text{C s}^{-1}$   
131 respectively, reaching 15 MPa and 1010  $^{\circ}\text{C}$  (Supplementary Table 3; Supplementary Fig. 6). The  
132 rapid decompression and cooling enabled large  $\Delta T$ s to be achieved ( $> 100 \text{ }^{\circ}\text{C}$ ; see  
133 Supplementary Fig. 6) in 300 s, favouring predominantly clinopyroxene crystallisation, with minor  
134 plagioclase and oxide (Supplementary Fig. 7). This indicates that  $\tau^{(c)}$  is  $< 60$  s, in agreement with  
135 the order of magnitude estimated from *in situ* experiments.

136 Large undercooling can produce significant syn-eruptive microlite crystallisation during rapid  
137 magma ascent<sup>24-27</sup>. This increase in crystallinity dramatically increases the viscosity of the  
138 magma<sup>19</sup>. This process has been proposed to explain explosive basaltic Plinian eruptions, supported  
139 by evidence of high microlite contents<sup>7-11,37,38</sup>. However, a mechanism for this exceptionally fast  
140 crystallisation during rapid magma ascent in basaltic Plinian eruptions, favouring fragmentation,  
141 has not been demonstrated so far.

142

### 143 **Numerical simulation of the 122 B.C. Etna basaltic Plinian eruption**

144 Magma fragmentation in basaltic Plinian eruptions has been investigated with conduit models,  
145 where crystallisation has been assumed either to be constant<sup>20</sup> or at equilibrium<sup>40</sup>. Recent results  
146 demonstrate that disequilibrium crystallisation plays a fundamental role in magma dynamics within

147 the conduit<sup>21</sup>, but syn-eruptive disequilibrium crystallisation has not yet been considered for basaltic  
148 explosive volcanism<sup>20,40</sup>.

149 We used the conduit model described by La Spina et al. (ref. 21, 23) to investigate the effect of  
150 the new experimentally constrained characteristic times for crystallisation with large undercooling  
151 derived here on the ductile-brittle transition of basaltic magma during highly explosive eruptions.  
152 Since we are focussing our attention on explosive eruptions with high mass eruption rates ( $>10^6$   
153 kg/s), it is reasonable to assume that outgassing is negligible for this kind of activity. Indeed,  
154 outgassing will be inhibited by fast magma ascent and fragmentation will be achieved faster than  
155 outgassing<sup>41</sup>. As a test case, we consider the 122 B.C. Etna basaltic Plinian eruption<sup>6-8</sup>. To model  
156 fragmentation we adopt the strain-rate criterion introduced by Papale (ref. 1):

$$157 \quad \dot{\gamma} = k \frac{G_{\infty}}{\mu} \quad (1)$$

158 where  $\dot{\gamma}$  is the elongational strain rate,  $k=0.01$  is a constant,  $\mu$  is the magmatic viscosity and  $G_{\infty}$   
159 is the elastic modulus at infinite frequency. The other constitutive equations are reported in the  
160 Methods section. In Figure 3 we report the calculated plagioclase undercooling, crystal content and  
161 viscosity as function of depth for  $\tau^{(c)} = 10$  and 1000 s. Large undercooling is produced by adiabatic  
162 expansion of exsolved volatiles, and mitigated by the latent heat of crystallisation for  $\tau^{(c)} = 10$  s  
163 (Fig. 3a). In this case, numerical results show a rapid increase in crystallinity and in viscosity at  
164 depths below 2 km (Fig. 3c), leading to fragmentation and explosive Plinian eruption. Importantly,  
165 numerical results indicate that strain-induced fragmentation is favoured by a combination of rapid  
166 viscosity increase (about one order of magnitude in 5 seconds approaching the fragmentation depth)  
167 and fast decompression/ascent rates ( $\sim 0.2$  MPa s<sup>-1</sup> and  $\sim 15$  m s<sup>-1</sup>) that generate high strain rates. For  
168  $\tau^{(c)} = 1000$  s, instead, the crystallisation rate is slow, and viscosity stays within the fragmentation  
169 threshold all along the conduit.

170

171 **Sensitivity analyses on basaltic magma fragmentation driven by rapid crystallisation**



172 Having established that fast crystallisation plays an important role on basaltic Plinian eruptions,  
173 we performed a sensitivity study with our numerical model to investigate the parameter space  
174 whereby basaltic fragmentation driven by rapid crystallisation may occur. We use the Etna 122 B.C.  
175 eruption as a test case. We focus on the behaviour of  $\Delta T$  as a function of characteristic time of  
176 crystallisation, pressure, temperature and magmatic H<sub>2</sub>O content at the conduit inlet, conduit radius,  
177 and initial phenocryst content. A detailed description of the initial condition of the sensitivity study  
178 can be found in the Methods section. We performed several sensitivity studies assuming a  
179 characteristic time of  $\tau^{(c)} = 10$  s, as observed in our experiments, and  $\tau^{(c)} = 1000$  s, as observed for  
180 Etna 2001 in mild explosive activity. We also examined  $\tau^{(c)} = 1$  and 100 s for completeness.

181 Numerical results show that undercooling is principally controlled by  $\tau^{(c)}$  (Fig. 4a), because the  
182 release of latent heat during rapid crystallisation (i.e. small  $\tau^{(c)}$ ) affects the temperature of the  
183 system, and, consequently, the undercooling. Therefore, undercooling and characteristic time are  
184 linked, affecting one each other. However, our numerical results indicate that, within the parameters  
185 space investigated,  $\Delta T$  is always maintained between 60 and 190 °C (Fig. 4b), which is enough to  
186 enable rapid crystallisation in any case. Furthermore, the sensitivity analyses indicate that, after the  
187 characteristic time, initial temperature and water content (exsolved + dissolved) play an important  
188 role on controlling undercooling (Fig. 4a).  $\Delta T$  at the point of fragmentation increases as initial  
189 temperature decreases (Fig. 4b), meaning that cooler magma in the chamber is more likely to  
190 produce microlite crystallisation during ascent, as  $\Delta T$  will already be large under the pre-eruptive  
191 condition. An increase in the initial total H<sub>2</sub>O (exsolved + dissolved) also produces an increase of  
192  $\Delta T$  (Fig. 4c), caused by greater cooling of the system due to enhanced adiabatic gas expansion.  
193 Furthermore, higher water content favours rapid crystallisation of microlites, due to the increase in  
194 diffusivity within the melt.

195 Our sensitivity studies show that a lower initial temperature and a higher pre-eruptive crystal  
196 content results in a greater likelihood of explosive eruptions (Fig. 4d,e). This is consistent with  
197 estimates of pre-eruptive temperatures obtained for the Etna and Fontana Plinian eruptions, which

198 range between 1000 and 1060 °C<sup>37</sup>. Regarding the pre-eruptive crystal content, however, products  
 199 erupted from basaltic Plinian eruptions are characterized by a small phenocryst content (<10  
 200 vol.%)<sup>7,8,10,11,37,38,40</sup>. Therefore, in this context of low initial temperature and low phenocryst  
 201 content, our results highlight that the characteristic time of crystallisation has a fundamental role on  
 202 the likelihood of producing an explosive eruption. Indeed, a small  $\tau^{(c)}$  is the primary cause for a  
 203 significant increase of the syn-eruptive crystal fraction over short timescales during magma ascent,  
 204 which consequently increases magma viscosity and, thus, the probability of magma fragmentation  
 205 (Fig. 4f). Moreover, our sensitivity analysis demonstrates that when the syn-eruptive crystal content  
 206 exceeds 30 vol.%, all numerical solutions reach the fragmentation threshold (Fig. 4f). Indeed, in a  
 207 fast ascending magma (from our sensitivity analyses we have an average ascent rate between ~5-50  
 208 m/s), this increase in syn-eruptive crystal content produces a rapid and dramatic increase of  
 209 viscosity (about one order of magnitude in less than 10 s close to the fragmentation depth),  
 210 increasing the likelihood of magma fragmentation. Numerical results also show that, as soon as  
 211 viscosity exceeds 10<sup>5</sup> Pa s, all the numerical solutions reach the fragmentation threshold, generating  
 212 an explosive eruption (Fig 4g). Indeed, for a fast ascending magma where outgassing can be  
 213 neglected and strain-rates are high, the key parameter controlling the triggering of fragmentation is  
 214 viscosity. Therefore, 10<sup>5</sup> Pa s represents a minimum viscosity determining a drastic change in  
 215 eruptive style for activities characterised by high mass eruption rates. This minimum viscosity is  
 216 one order of magnitude lower than previously reported for low-viscosity magmas<sup>1,42</sup>.

217 Experimental and natural observations combined with a numerical model allow us to conclude  
 218 that pre-eruptive temperatures <1100 °C favour the formation of highly explosive basaltic  
 219 eruptions, such as Plinian volcanism, driven by fast syn-eruptive crystal growth under high  
 220 undercooling. This implies that all basaltic systems on Earth have the potential to produce powerful  
 221 explosive eruptions.

## METHODS

**Starting material.** The starting material, used for our crystallisation experiments, is a trachybasalt from the lower vents of the 2001 Mt. Etna eruption<sup>36,43</sup>. The anhydrous, glassy starting material was obtained by melting crushed rock samples in a Pt crucible. Melting was performed in a Nabertherm® MoSi<sub>2</sub> box furnace at 1400 °C and at atmospheric pressure. The melt was left in the furnace for four hours to allow the melt to fully degas and to dissolve the crystals present. The melt was then quenched in air to glass. This procedure was repeated two times to homogenise the melt. Finally, anhydrous glassy cylinders 3 mm in diameter and 4 mm in length were drilled from the synthesized glass for *ex situ* and *in situ* 4D crystallisation experiments.

The chemical composition of the anhydrous glassy starting material has been analysed with a Jeol JXA 8530 F microprobe at the Photon Science Institute, University of Manchester, Manchester, UK, and are reported in Supplementary Table 1. Analyses were performed using a 15 kV accelerating voltage, 10 nA beam current and beam size of 10 µm. Standards used for calibration were albite for Na, periclase for Mg, corundum for Al, fayalite for Fe, tephroite for Mn, apatite for P, sanidine for K, wollastonite for Ca and Si and rutile for Ti. Sodium and potassium were measured first to minimize loss owing to volatilisation.

Hydrous trachybasaltic glass with ~3 wt. % of H<sub>2</sub>O was obtained melting the starting material and homogenizing H<sub>2</sub>O in a Pt capsule at 100 MPa and 1200 °C. The hydrous starting glasses were produced using a TZM cold seal pressure vessel apparatus at the School of Earth Sciences, University of Bristol, Bristol, UK. Before to perform crystallisation experiments Raman spectra were collected from the hydrous starting glass, using a Thermo Scientific™ DXRTMxi Raman Imaging Microscope at the School of Earth Sciences, University of Bristol (Bristol, UK) in order to check that the amount of H<sub>2</sub>O was ~3 wt. %.

***Ex situ* decompression and cooling experiments.**

*Ex situ* experiments were performed in order to investigate the process of fast crystallisation in a hydrous trachybasaltic melt during a continuous decompression ( $0.2 \text{ MPa s}^{-1}$ ) and cooling ( $0.2 \text{ }^{\circ}\text{Cs}^{-1}$ ), simulating magma ascent in the conduit. Two experiments were performed using a TZM cold seal pressure vessel apparatus at the School of Earth Sciences, University of Bristol, Bristol, UK. The redox condition of the apparatus was NNO, adding ~1 vol.% of hydrogen to the pressuring argon. Capsules ( $\text{Au}_{80}\text{-Pd}_{20}$ ) were loaded with hydrous glass with a cylindrical shape. The experimental approach consisted of holding the sample for 30 minutes at 75 MPa and  $1070 \text{ }^{\circ}\text{C}$  before being decompressed and cooled. The first experiment was quenched after 30 minutes at 75 MPa and  $1070 \text{ }^{\circ}\text{C}$ , in order to texturally characterise the initial conditions before that fast decompression and cooling were applied. In the second experiment, after 30 minutes pressure and temperature were released continuously in 300 s at  $0.2 \text{ MPa s}^{-1}$  and  $0.2 \text{ }^{\circ}\text{Cs}^{-1}$  respectively, reaching 15 MPa and  $1010 \text{ }^{\circ}\text{C}$  (Supplementary Table 3; Supplementary Fig. 6). The sample was rapidly quenched at the final conditions. Final pressure was chosen as approximate fragmentation pressures calculated by modeling. Decompression and cooling rates were predicted from the conduit model for magma ascent during basaltic Plinian eruptions.

***In situ* synchrotron X-ray microtomography experiments.** The experiments were performed at the beamline I12-JEEP<sup>44</sup>, Diamond Light Source, Harwell, UK. For these *in situ* crystallisation experiments, we used the high-temperature resistance Alice furnace<sup>45</sup>, which allows us to control cooling at  $0.05 \text{ }^{\circ}\text{Cs}^{-1}$  to  $0.4 \text{ }^{\circ}\text{Cs}^{-1}$ , and the P2R in situ rig<sup>35</sup> for high speed rotation. Temperature was measured with a R type thermocouple, which was close to the sample, positioned in the middle of the hot spot. The dimension of the Alice furnace's hot spot with homogeneous temperature is ~5x5x5 mm; our samples were positioned within this area. The R type thermocouple provided us the temperature of the sample with an uncertainty of  $\pm 5 \text{ }^{\circ}\text{C}$ . The sample holder was an alumina crucible (Supplementary Fig. 2), which is suitable for the temperature range investigated and it has low X-ray attenuation coefficient. The glassy cylinders were heated *in situ* in the Alice furnace up

273 to 1250 °C for 30 minutes (Supplementary Figure 1). After the initial annealing period,  
274 crystallisation was induced by decreasing temperature from 1250 °C to 1170 °C or 1150 °C at  
275 ambient pressure, holding at the final temperature for 4 h<sup>36</sup> (Supplementary Figure 1). After this  
276 step, the system was perturbed by a rapid cooling at rate of 0.4 °Cs<sup>-1</sup> in order to investigate the rapid  
277 crystallisation in real time (Supplementary Figure 1), reaching high undercooling (up to ~180 °C) in  
278 a short time.

279 The experiments were performed in phase-contrast mode, setting the sample-to-detector distance  
280 at 2300 mm in order to work in the edge-detection regime<sup>46</sup> (Supplementary Table 4). The  
281 projections were acquired using a monochromatic X-ray beam with energy of 53 keV. In each scan,  
282 1800 tomographic projections were acquired by the detector with equiangular steps over a full  
283 rotation angle of 180° (Supplementary Table 4). The exposure time for the acquisition of each  
284 projection was 0.05 s (Supplementary Table 4), therefore, the temporal resolution of each scan was  
285 of 90 seconds. The isotropic pixel size is 3.2 µm. The detector was a high-resolution imaging PCO  
286 edge camera with optical module 3, corresponding to a field of view of 8.0 mm × 7.0 mm. Scan  
287 acquisition started before the end of the annealing, covering the cooling period between 1250 °C  
288 and the dwell temperatures (1170 and 1150 °C), the entire duration of the dwell time and the final  
289 rapid cooling rate of 0.4 °Cs<sup>-1</sup>.

290

291 **Image reconstruction and processing.** Tomographic projections were reconstructed into 32-bit  
292 slices by using Diamond I12 in-house python codes, using the *gridrec* algorithm<sup>47,48</sup>  
293 ([http://confluence.diamond.ac.uk/display/I12Tech/Reconstruction+](http://confluence.diamond.ac.uk/display/I12Tech/Reconstruction+scripts+for+time+series+tomography)  
294 [scripts+for+time+series+tomography](http://confluence.diamond.ac.uk/display/I12Tech/Reconstruction+scripts+for+time+series+tomography))<sup>49,50</sup>. The pre-processing pipeline includes centre of rotation  
295 calculation<sup>49</sup>, zinger removal, blob removal<sup>50</sup>, and regularisation-based ring removal<sup>51</sup>.

296 The reconstructed slices were converted to 8-bit raw format and stacked using ImageJ software<sup>52</sup>  
297 to obtain volumes in which the isotropic voxel has an edge size of 3.2 µm. Reconstructed volumes  
298 of experiments ET1150 and ET1170 were then cropped using Avizo® software v.8.0 (FEI

Visualization Sciences Group) in order to select the volume of interest (VOI) (Supplementary Table 4). In the experiment ET1150 plagioclase and pyroxene crystals nucleated and grew in a relatively large pocket of melt (Figs 1 and 2). Therefore, the VOI selected consists of a volume of melt where the rapid crystallisation of plagioclase and pyroxene occurred during the final rapid cooling rate of  $0.4\text{ }^{\circ}\text{Cs}^{-1}$ . In the experiment ET1170 plagioclase and pyroxene crystals formed in narrow layers of melt (Supplementary Fig. 3), during rapid continuous cooling at a rate of  $0.4\text{ }^{\circ}\text{Cs}^{-1}$ .

Three-dimensional visualization (volume rendering) of the reconstructed volumes was obtained using the commercial software VGStudio 3.0 (Volume Graphics), which allowed us to make 3D textural observations of the plagioclase and pyroxene crystal morphologies (Fig. 2). Therefore, the reconstructed volume of each scan allowed us to quantify when and at which range of temperature plagioclase and pyroxene crystals were able to form.

**Image segmentation and analysis of plagioclase.** Segmentation is the process that allows separation of objects from the background to obtain binary volumes containing only the feature of interest. Segmentation of plagioclase crystals from the glassy matrix was performed using the semi-automatic volume segmentation<sup>53,54</sup> in Avizo software v. 8.0 (Supplementary Table 4). This segmentation requires manual drawing of the outlines of crystals on the 2D slices. This is repeated every 5–10 slices, depending on the size of the crystal and the complexity of their shape, along the crystal length. The crystal shape is reconstructed automatically by the software through an interpolation procedure. The advantage of this technique is that the operator can obtain the real morphology of the object of interest by visual inspection<sup>53,54</sup>.

The reconstructed 3D images were processed and analysed with the Pore3D software library, custom-developed at Elettra<sup>55</sup>. The Pore3D software allowed us to quantify the number of plagioclase crystals, the volume and the maximum length of each crystal, operating directly in the 3D domain<sup>55,56</sup>. As we were able to obtain the 3D shape of plagioclase crystals and the real maximum axis length ( $L_{3D}$ ) we could calculate the growth rate ( $Y_{L3D}$ ) of plagioclase crystals

325 (Supplementary Table 2), using the experimental duration of growth (experimental duration). The  
326 growth rate was estimated using the following equation<sup>53</sup>:

327 
$$Y_{L3D} = (L_{3D} * 0.5) / t_{\text{growth}}$$

328 where  $t_{\text{growth}}$  is the time required for crystal growth. The microtomography images give us the  
329 opportunity to measure the volume of crystals. The volumetric growth rate ( $Y_v$ ) was calculated  
330 (Supplementary Table 2) using the following relationship<sup>53</sup>:

331 
$$Y_v = (V * 0.5) / t_{\text{exp}}$$

332 where  $V$  is the volume of the crystal.

333

334 **Image analysis of pyroxene growth kinetics.** Back-scattered electron (BSE) images were  
335 collected, using a JEOL JSM-6390LA FE-SEM at the School of Earth and Environmental Sciences,  
336 University of Manchester, Manchester, UK, in order to analyse the pyroxene morphologies and  
337 kinetics. We used an acceleration voltage of 15 kV and beam current of 10 nA. The sizes of  
338 dendritic pyroxene crystals were measured in the 2D domain, using BSE images and ImageJ  
339 software<sup>52</sup>, as pyroxene morphologies formed during continuous cooling are difficult to resolve and  
340 analyse in the 3D domain. The pyroxene growth rate is calculated by dividing the entire length of  
341 the dendritic crystal over the duration of the pyroxene growth (Supplementary Table 2), as dendritic  
342 crystals grow in one direction.

343

344 **Electron microprobe analysis.** Samples obtained with *ex situ* and *in situ* crystallisation  
345 experiments were analysed with a JEOL JXA-8530F field emission electron microprobe at the  
346 Photon Science Institute, University of Manchester, Manchester, UK. For both instruments, the  
347 operating conditions were as follows: 15 kV accelerating voltage, 10 nA beam current, and beam  
348 diameter of 10 or 5  $\mu\text{m}$  (the latter for microlites). Sodium and potassium were measured first to  
349 minimise loss by volatilisation. Calibration standards were albite for Na, periclase for Mg,  
350 corundum for Al, fayalite for Fe, tephroite for Mn, apatite for P, sanidine for K, wollastonite for Ca

351 and Si and rutile for Ti. Several compositional maps, with a nominal resolution of 1  $\mu\text{m}^2$ , have been  
 352 also collected using the EPMA (EPMA map, are reported in Supplementary Figs. 4, 5 and 7).

353

354 **Constitutive equations for the conduit model.** In this work we use the 1D steady-state model  
 355 for magma ascent described by ref. (21, 23, 57). The governing equations used in this work are  
 356 reported in ref. (57). The application to a specific volcano is achieved by providing constitutive  
 357 equations to describe the specific rheological, solubility, crystallisation, outgassing, and  
 358 fragmentation behaviour of the system.

359 Following ref. (58), the viscosity of the liquid phase is modelled as:

360 
$$\mu_l = \mu_{melt} \cdot \theta(x_c^l),$$

361 where  $\mu_{melt}$  is the viscosity of the bubble-free, crystal-free liquid phase and  $\theta$  is a factor which  
 362 increases viscosity attributed to the presence of crystals<sup>59</sup>.

363 We use an empirical relationship to estimate  $\mu_{melt}$  as a function of water concentration and  
 364 temperature, as in ref. (60) (based on the Vogel-Fulcher-Tammann equation):

365 
$$\log(\mu_{melt}) = A + \frac{B(y, x_{d_{H_2O}}^{md})}{T - C(y, x_{d_{H_2O}}^{md})},$$

366 where the viscosity  $\mu_{melt}$  is in Pa s and  $T$  is the temperature in Kelvin. The parameter  $A$  is the  
 367 logarithmic value of the viscosity at infinite temperature and it is assumed to be constant for all  
 368 melts. The parameters  $B$  and  $C$ , instead, are functions of the melt composition  $y$  and of the dissolved  
 369 water content  $x_{d_{H_2O}}^{md}$ . In this work, we used the composition of the average melt inclusion  
 370 composition (Etna 122 B.C.) from ref. (61). Furthermore, as crystallisation proceeds, viscosity is  
 371 increased according to the empirical model described in ref. (62):

372 
$$\theta = \frac{1 + \varphi^\delta}{[1 - F(\varphi, \xi, \gamma)]^{B\phi^*}},$$

373 where



$$F = (1 - \xi) \operatorname{erf} \left[ \frac{\sqrt{\pi}}{2(1 - \xi)} \varphi(1 + \varphi^\gamma) \right], \quad \varphi = \frac{\left( \sum_{j=1}^{n_c} x_{c_j}^l \right)}{\phi^*}.$$

The fitting parameters  $B, \delta, \xi, \gamma$  and  $\phi^*$  chosen for this work are the same used in ref. (63).

The model proposed in this work takes into account two different gas components: water and carbon dioxide. The equilibrium profile of the dissolved gas content  $x_{d_i}^{md,eq}$  of component  $i$  follows the Henry's Law, i.e.

$$x_{d_i}^{md,eq} = \sigma_i \left( \frac{P_{g,i}}{\bar{P}} \right)^{\varepsilon_i},$$

where  $P_{g,i} = \alpha_{g_i} P_g / \alpha_g$  is the partial pressure of the  $i$ -th gas component expressed in  $Pa$ ,  $\bar{P} = 1$  Pa is used to make the expression in the brackets adimensional,  $\sigma_i$  is the solubility coefficient and  $\varepsilon_i$  is the solubility exponent. We assume that the solubility parameter  $\sigma_i$  and  $\varepsilon_i$  are constant during ascent. For this work we adopted the following parameters  $\sigma_{H_2O} = 1.8911 \times 10^{-6}$ ;  $\varepsilon_{H_2O} = 0.5257$ ;  $\sigma_{CO_2} = 2.2154 \times 10^{-12}$ ;  $\varepsilon_{CO_2} = 1.075$ . In this work, we assume also equilibrium exsolution, which means that the dissolved volatile contents always follow the equilibrium profile.

The crystallisation model adopted here has been proposed in ref. (23). We consider the three different major crystal components erupted by Etna volcano: plagioclase, pyroxene and olivine. We assume that crystals stay coupled with the melt (i.e. no fractional crystallisation). For a better modelling of crystal nucleation and growth, we also assume that the equilibrium crystal contents are functions of temperature, pressure and dissolved water content. With these assumptions, the equilibrium mass fraction  $x_{c_j}^{l,eq}$  of crystal phase  $j$  is computed using the polynomial function

$$\begin{aligned} x_{c_j}^{l,eq}(P^*, T^*, x_d^*) = & \zeta_{j,1}(P^*)^2 + \zeta_{j,2}(T^*)^2 + \zeta_{j,3}(x_d^*)^2 + \zeta_{j,4}(P^*)(T^*) + \\ & + \zeta_{j,5}(T^*)(x_d^*) + \zeta_{j,6}(x_d^*)(P^*) + \zeta_{j,7}(P^*) + \zeta_{j,8}(T^*) + \zeta_{j,9}(x_d^*) + \zeta_{j,10}, \end{aligned}$$

where  $P^*$  is the liquid pressure expressed in bars,  $T^*$  is the temperature expressed in Celsius degrees and  $x_d^*$  is the dissolved water concentration in weight percent. From  $x_{c_j}^{l,eq}$ , the equilibrium crystal volume fraction  $\beta_j^{eq}$  can be computed using the relation

$$\beta_j^{eq} = \frac{\rho_l x_{c_j}^{l,eq}}{\rho_{c_j}}.$$

The parameters  $\zeta_{j,i}$  are calculated fitting the polynomial function over a large range of data obtained at different pressures, temperatures and water contents with alphaMELTS<sup>64</sup>, a command line version of MELTS<sup>65</sup>. As previously, we used the average melt inclusion composition (Etna 122 B.C.) from ref. (61).

Disequilibrium crystallisation is considered in our model and characteristic times controls the time needed to reach equilibrium crystal content. The differential equation in the conduit model which describes the crystal volume fraction within the conduit is the following<sup>21</sup>:

$$\frac{\partial \alpha_l \rho_c \beta u_l}{\partial z} = -\frac{1}{\tau^{(c)}} \alpha_l \rho_c (\beta - \beta^{eq}).$$

Here,  $\alpha_l$  is the volume fraction of the liquid phase,  $\rho_c$  is the density of the crystals,  $u_l$  is the velocity of the liquid phase,  $z$  is the vertical axis,  $\beta$  is the actual total crystal volume fraction, whereas  $\beta^{eq}$  is the equilibrium total crystal volume fraction. If we multiply all the terms by the characteristic time  $\tau^{(c)}$ , we notice that the smaller is  $\tau^{(c)}$ , the smaller has to be  $(\beta - \beta^{eq})$ . In other terms, the smaller is the characteristic time, the faster the crystals will reach the equilibrium value.

Formally, as described in La Spina et al. (ref. 21), the characteristic time reflects the time required to reduce the difference between the actual and the equilibrium value to  $e^{-1}$  (~37%) of the initial difference. This means that, if  $\beta_0$  is the initial value of a physical parameter  $\beta$  (which, in our case, is the crystal volume fraction), and  $\beta_{eq}$  is the equilibrium value in response to a perturbation of the system, at the characteristic time  $\tau$ , we have

$$\beta(\tau) = \beta^{eq} + e^{-1}(\beta_0 - \beta^{eq}).$$

The experimental phase diagram for Etna basalt erupted during the 122 B.C. eruption<sup>37</sup> provides the plagioclase and pyroxene liquidus at different pressures and temperatures, whilst the conduit model is able to track temperature evolution within the conduit. Combining both of these data, we can estimate  $\Delta T$  with respect to the plagioclase and pyroxene liquidus during magma ascent.

420 For this work, as we are interested in the highly explosive activity, we assumed no relative  
421 velocity between gas and melt. Furthermore, as we indicated in the main text, we used as  
422 fragmentation model the strain-rate criterion introduced by ref. (1).

423

424 **Initial condition for the sensitivity analysis.**

425 The range of input parameters adopted for the sensitivity analysis are the following: 140–160  
426 MPa for the inlet pressure at 6000 m depth, 1050–1100 °C for the magma inlet temperature, 5–30 m  
427 for the radius of the conduit, 2.0–4.0 wt.% for the total water content, 0.1–2.0 wt.% for the total  
428 CO<sub>2</sub> content, 0–20 vol.% for the initial phenocrysts, and 1–1000 s for the characteristic time of  
429 crystallisation. As we do not know the probability distribution of the uncertain input parameters,  
430 we have assumed a uniform distribution within the aforementioned ranges. The sensitivity analysis  
431 was performed on using the DAKOTA toolkit (Design Analysis Kit for Optimization and Terascale  
432 Applications)<sup>66</sup>, an open-source software developed at Sandia National Laboratories that provides a  
433 flexible and extensible interface between analysis codes and iterative systems analysis methods  
434 such as uncertainty quantification, sensitivity analysis, optimization, and parameter estimation.

## References

1. Papale, P. Strain-induced magma fragmentation in explosive eruptions. *Nature* **397**, 425 (1999).
2. Dingwell, D. B. (1996). Volcanic Dilemma--Flow or Blow?. *Science*, 273(5278), 1054-1055.
3. Carey, S., & Sigurdsson, H. (1989). The intensity of plinian eruptions. *Bulletin of Volcanology*, 51(1), 28-40.
4. Wilson, L. (1976). Explosive volcanic eruptions—III. Plinian eruption columns. *Geophysical Journal International*, 45(3), 543-556.
5. Polacci, M., Corsaro, R. A. & Andronico, D. Coupled textural and compositional characterization of basaltic scoria: Insights into the transition from Strombolian to fire fountain activity at Mount Etna, Italy. *Geology* **34**, 201-204 (2006).
6. Coltelli, M., Del Carlo, P. & Vezzoli, L. Discovery of a Plinian basaltic eruption of Roman age at Etna volcano, Italy. *Geology* **26**, 1095-1098 (1998).
7. Houghton, B. F., Wilson, C. J. N., Del Carlo, P., Coltelli, M., Sable, J. E. & Carey, R. The influence of conduit processes on changes in style of basaltic Plinian eruptions: Tarawera 1886 and Etna 122 BC. *Journal of Volcanology and Geothermal Research* **137**, 1-14 (2004).
8. Sable, J. E., Houghton, B. F., Del Carlo, P. & Coltelli, M. Changing conditions of magma ascent and fragmentation during the Etna 122 BC basaltic Plinian eruption: Evidence from clast microtextures. *Journal of Volcanology and Geothermal Research* **158**, 333-354 (2006).
9. Houghton, B. F. & Gonnermann, H. M. Basaltic explosive volcanism: constraints from deposits and models. *Chemie der Erde-Geochemistry* **68**, 117-140 (2008).
10. Sable, J. E. Houghton, B. F., Wilson, C. J. N. & Carey, R. J. Eruption mechanisms during the climax of the Tarawera 1886 basaltic Plinian eruption inferred from microtextural characteristics of the deposits. *Studies in Volcanology: The Legacy of George Walker. Special Publications of IAVCEI* **2**, 129-154 (2009).

- 460 11. Costantini, L., Houghton, B. F. & Bonadonna, C. Constraints on eruption dynamics of  
461 basaltic explosive activity derived from chemical and microtextural study: the example of the  
462 Fontana Lapilli Plinian eruption, Nicaragua. *Journal of Volcanology and Geothermal Research* **189**,  
463 207-224 (2010).
- 464 12. Melnik, O., & Sparks, R. S. J. (1999). Nonlinear dynamics of lava dome extrusion. *Nature*,  
465 402(6757), 37.
- 466 13. Gonnermann, H. M., & Manga, M. (2003). Explosive volcanism may not be an inevitable  
467 consequence of magma fragmentation. *Nature*, 426(6965), 432.
- 468 14. Gonnermann, H. M. (2015). Magma fragmentation. *Annual Review of Earth and Planetary*  
469 *Sciences*, 43, 431-458.
- 470 15. Alidibirov, M., & Dingwell, D. B. (1996). Magma fragmentation by rapid decompression.  
471 *Nature*, 380(6570), 146.
- 472 16. Zhang, Y. (1999). A criterion for the fragmentation of bubbly magma based on brittle failure  
473 theory. *Nature*, 402(6762), 648.
- 474 17. Spieler, O., Kennedy, B., Kueppers, U., Dingwell, D. B., Scheu, B., & Taddeucci, J. (2004).  
475 The fragmentation threshold of pyroclastic rocks. *Earth and Planetary Science Letters*, 226(1-2),  
476 139-148.
- 477 18. Kueppers, U., Scheu, B., Spieler, O., & Dingwell, D. B. (2006). Fragmentation efficiency of  
478 explosive volcanic eruptions: A study of experimentally generated pyroclasts. *Journal of*  
479 *Volcanology and Geothermal Research*, 153(1-2), 125-135.
- 480 19. Giordano, D. & Dingwell, D. Viscosity of hydrous Etna basalt: implications for Plinian-style  
481 basaltic eruptions. *Bulletin of Volcanology* **65**, 8-14 (2003).
- 482 20. Moitra, P., Gonnermann, H. M., Houghton, B. F. & Tiwary, C. S. Fragmentation and Plinian  
483 eruption of crystallizing basaltic magma. *Earth and Planetary Science Letters* **500**, 97-104 (2018).

- 484 21. La Spina, G., Burton, M., Vitturi, M. D. M. & Arzilli, F. Role of syn-eruptive plagioclase  
485 disequilibrium crystallisation in basaltic magma ascent dynamics. *Nature communications* **7**, 13402  
486 (2016).
- 487 22. Cashman, K. & Blundy, J. Degassing and crystallisation of ascending andesite and  
488 dacite. *Philosophical Transactions of the Royal Society of London A: Mathematical, Physical and*  
489 *Engineering Sciences* **358**, 1487-1513 (2000).
- 490 23. La Spina, G., Burton, M., de' Michieli Vitturi, M. Temperature evolution during magma  
491 ascent in basaltic effusive eruptions: a numerical application to Stromboli volcano. *Earth Planet.*  
492 *Sci. Lett.* **426**, 89–100 (2015).
- 493 24. Hammer, J. E. & Rutherford, M. J. An experimental study of the kinetics of decompression-  
494 induced crystallization in silicic melt. *Journal of Geophysical Research: Solid Earth* **107**, ECV-8  
495 (2002).
- 496 25. Couch, S., Harford, C. L., Sparks, R. S. J. & Carroll, M. R. Experimental constraints on the  
497 conditions of formation of highly calcic plagioclase microlites at the Soufriere Hills Volcano,  
498 Montserrat. *Journal of Petrology* **44**, 1455-1475 (2003).
- 499 26. Shea, T. & Hammer, J. E. Kinetics of cooling-and decompression-induced crystallization in  
500 hydrous mafic-intermediate magmas. *Journal of Volcanology and Geothermal research* **260**, 127-  
501 145 (2013).
- 502 27. Agostini, C., Fortunati, A., Arzilli, F., Landi, P. & Carroll, M. R. Kinetics of crystal  
503 evolution as a probe to magmatism at Stromboli (Aeolian Archipelago, Italy). *Geochimica et*  
504 *cosmochimica acta* **110**, 135-151 (2013).
- 505 28. Vona, A. & Romano, C. The effects of undercooling and deformation rates on the  
506 crystallization kinetics of Stromboli and Etna basalts. *Contributions to Mineralogy and*  
507 *Petrology* **166**, 491-509 (2013).

- 508 29. Kolzenburg, S., Giordano, D., Hess, K. U. & Dingwell, D. B. Shear Rate-Dependent  
509 Disequilibrium Rheology and Dynamics of Basalt Solidification. *Geophysical Research Letters* **45**,  
510 6466-6475 (2018).
- 511 30. Marsh, B. D. (1998). On the interpretation of crystal size distributions in magmatic  
512 systems. *Journal of Petrology*, 39(4), 553-599.
- 513 31. Cashman, K. V. Relationship between plagioclase crystallization and cooling rate in basaltic  
514 melts. *Contributions to Mineralogy and Petrology* **113**, 126-142 (1993).
- 515 32. Conte, A. M., Perinelli, C. & Trigila, R. Cooling kinetics experiments on different Stromboli  
516 lavas: Effects on crystal morphologies and phases composition. *Journal of Volcanology and*  
517 *Geothermal Research* **155**, 179-200 (2006).
- 518 33. Szramek, L., Gardner, J. E. & Hort, M. Cooling-induced crystallization of microlite crystals  
519 in two basaltic pumice clasts. *American Mineralogist* **95**, 503-509 (2010).
- 520 34. Brugger, C. R. & Hammer, J. E. Crystallization kinetics in continuous decompression  
521 experiments: implications for interpreting natural magma ascent processes. *Journal of Petrology* **51**,  
522 1941-1965 (2010).
- 523 35. Karagadde, S., Lee, P. D., Cai, B., Fife, J. L., Azeem, M. A., Kareh, K. M., Puncreobutr, C.,  
524 Tsivoulas, D., Connolley, T. & Atwood, R. C. Transgranular liquation cracking of grains in the  
525 semi-solid state. *Nature communications* **6**, 8300 (2015).
- 526 36. Polacci, M., Arzilli, F., La Spina, G., Le Gall, N., Cai, B., Hartley, M. E., Di Genova, D., Vo,  
527 N. T., Nonni, S., Atwood, R. C., Llewellyn, E. W., Lee, P. D. & Burton, M. R. Crystallisation in  
528 basaltic magmas revealed via in situ 4D synchrotron X-ray microtomography. *Scientific Reports* **8**,  
529 8377 (2018).
- 530 37. Goepfert, K. & Gardner, J. E. Influence of pre-eruptive storage conditions and volatile  
531 contents on explosive Plinian style eruptions of basic magma. *Bulletin of Volcanology* **72**, 511-521  
532 (2010).

- 533 38. Szramek, L. A. Mafic Plinian eruptions: Is fast ascent required? *Journal of Geophysical*  
534 *Research: Solid Earth* **121**, 7119-7136 (2016).
- 535 39. Suzuki, Y. & Fujii, T. Effect of syneruptive decompression path on shifting intensity in  
536 basaltic sub-Plinian eruption: Implication of microlites in Yufune-2 scoria from Fuji volcano, Japan.  
537 *Journal of Volcanology and Geothermal Research*, **198**, 158-176 (2010).
- 538 40. Campagnola, S., Romano, C., Mastin, L. G. & Vona, A. Confort 15 model of conduit  
539 dynamics: applications to Pantelleria Green Tuff and Etna 122 BC eruptions. *Contributions to*  
540 *Mineralogy and Petrology* **171**, 60 (2016).
- 541 41. Cassidy, M., Manga, M., Cashman, K., & Bachmann, O. (2018). Controls on explosive-  
542 effusive volcanic eruption styles. *Nature communications*, 9, 2839.
- 543 42. Namiki, A. & Manga, M. Transition between fragmentation and permeable outgassing of low  
544 viscosity magmas. *Journal of Volcanology and Geothermal Research* **169**, 48-60 (2008).
- 545
- 546
- 547 43. Corsaro, R. A., Miraglia, L. & Pompilio, M. Petrologic evidence of a complex plumbing  
548 system feeding the July-August 2001 eruption of Mt. Etna, Sicily, Italy. *B. Volcanol.* **69**, 401–421  
549 (2007).
- 550 44. Drakopoulos, M., Connolley, T., Reinhard, C., Atwood, R., Magdysyuk, O., Vo, N., Hart,  
551 M., Connor, L., Humphreys, B., Howell, G. & Davies, S. I12: the joint engineering, environment  
552 and processing (JEEP) beamline at diamond light source. *Journal of synchrotron radiation* **22**, 828-  
553 838 (2015).
- 554 45. Azeem, M. A., Lee, P. D., Phillion, A. B., Karagadde, S., Rockett, P., Atwood, R. C.,  
555 Courtois, L., Rahman, K. M. & Dye, D. Revealing dendritic pattern formation in Ni, Fe and Co  
556 alloys using synchrotron tomography. *Acta Materialia* **128**, 241-248 (2017).
- 557 46. Cloetens, P., Barrett, R., Baruchel, J., Guigay, J. P. & Schlenker, M. Phase objects in syn-  
558 chrotron radiation hard X-ray imaging. *J. Phys. D. Appl. Phys.* **29**, 133–46 (1996).



559 47. O'sullivan, J. D. A fast sinc function gridding algorithm for Fourier inversion in computer  
560 tomography. *IEEE transactions on medical imaging* **4**, 200-207 (1985).

561 48. Gürsoy, D., De Carlo, F., Xiao, X. & Jacobsen, C. TomoPy: a framework for the analysis of  
562 synchrotron tomographic data. *Journal of synchrotron radiation* **21**, 1188-1193 (2014).

563 49. Vo, N. T., Drakopoulos, M., Atwood, R. C. & Reinhard, C. Reliable method for calculating  
564 the center of rotation in parallel-beam tomography. *Opt. Express* **22**, 19078–19086 (2014).

565 50. Vo, N. T., Atwood, R. C. and Drakopoulos, M. Superior techniques for eliminating ring  
566 artifacts in X-ray micro-tomography. *Optics express* **26**, 28396-28412 (2018).

567 51. Titarenko, S., Withers, P. J. & Yagola, A. An analytical formula for ring artefact suppression  
568 in X-ray tomography. *Applied Mathematics Letters* **23**, 1489-1495 (2010).

569 52. Abramoff M. D., Magalhaes P. J., Ram S. J. Image processing with ImageJ. *Biophot. Int.* **11**,  
570 36–42 (2004).

571 53. Arzilli, F., Mancini, L., Voltolini, M., Cicconi, M. R., Mohammadi, S., Giuli, G., Mainprice,  
572 D., Paris, E., Barou, F. & Carroll, M. R. Near-liquidus growth of feldspar spherulites in trachytic  
573 melts: 3D morphologies and implications in crystallization mechanisms. *Lithos* **216**, 93-105 (2015).

574 54. Arzilli, F., Polacci, M., Landi, P., Giordano, D., Baker, D. R. & Mancini, L. A novel protocol  
575 for resolving feldspar crystals in synchrotron X-ray microtomographic images of crystallized  
576 natural magmas and synthetic analogs. *American Mineralogist* **101**, 2301-2311 (2016).

577 55. Brun, F., Mancini, L., Kasae, P., Favretto, S., Dreossi, D. & Tromba, G. Pore3D: a software  
578 library for quantitative analysis of porous media. *Nucl. Instrum. Meth. A* **615**, 326–332 (2010).

579 56. Ohser, J. & Mücklich, F. Statistical analysis of microstructure in material science. Barnett V,  
580 editor. *Statistics in Practice*, West Sussex, England: John Wiley & Sons; (2000).

581 57. La Spina, G., Polacci, M., Burton, M. & de' Michieli Vitturi, M. Numerical investigation of  
582 permeability models for low viscosity magmas: application to the 2007 Stromboli effusive eruption  
583 *Earth and Planetary Science Letters* **473**, 279-290 (2017).

- 584 58. de' Michieli Vitturi, M., Clarke, A. B., Neri, A. & Voight, B. Transient effects of magma  
585 ascent dynamics along a geometrically variable dome-feeding conduit. *Earth Planet. Sci. Lett.* **295**,  
586 541–553 (2010).
- 587 59. Caricchi, L., Burlini, L., Ulmer, P., Gerya, T., Vassalli, M. & Papale, P. Non-Newtonian  
588 rheology of crystal-bearing magmas and implications for magma ascent dynamics. *Earth Planet.*  
589 *Sci. Lett.* **264**, 402–419 (2007).
- 590 60. Giordano, D., Russell, J. K. & Dingwell, D. B. Viscosity of magmatic liquids: a model. *Earth*  
591 *Planet. Sci. Lett.* **271**, 123–134 (2008).
- 592 61. Del Carlo, P. & Pompilio, M. The relationship between volatile content and the eruptive style  
593 of basaltic magma: the Etna case. *Annals of Geophysics*, **47** (2004).
- 594 62. Costa, A., Caricchi, L. & Bagdassarov, N. A model for the rheology of particle-bearing  
595 suspensions and partially molten rocks. *Geochem. Geophys. Geosyst.* **10**, (2009).
- 596 63. Vona, A., Romano, C., Dingwell, D. & Giordano, D. The rheology of crystal-bearing basaltic  
597 magmas from Stromboli and Etna. *Geochim. Cosmochim. Acta* **75**, 3214–3236 (2011).
- 598 64. Smith, P. M. & Asimow, P. D. Adibat\_1ph: a new public front-end to the MELTS,  
599 pMELTS, and pHMELTS models. *Geochem. Geophys. Geosyst.* **6**, (2005).
- 600 65. Ghiorso, M. S. & Sack, R. O. Chemical mass transfer in magmatic processes IV. A revised  
601 and internally consistent thermodynamic model for the interpolation and extrapolation of liquid–  
602 solid equilibria in magmatic systems at elevated temperatures and pressures. *Contrib. Mineral.*  
603 *Petrol.* **119**, 197–212 (1995).
- 604 66. Adams, B. M., Ebeida, M. S., Eldred, M. S., Geraci, G., Jakeman, J. D., Maupin, K. A.,  
605 Monschke, J. A., Swiler, L. P., Stephens, J. A., Vigil, D. M., Wildey, T. M., Bohnhoff, W. J.,  
606 Dalbey, K. R., Eddy, J. P., Frye, J. R., Hooper, R. W., Hu, K. T., Hough, P. D., Khalil, M.,  
607 Ridgway, E. M. & Rushdi, A. DAKOTA, A Multilevel Parallel Object-Oriented Framework for  
608 Design Optimization, Parameter Estimation, Uncertainty Quantification, and Sensitivity Analysis  
609 Version 6.6 User's Manual Tech. rep., SAND2014-4633, Tech. rep., SAND2014-4633, (2017).

**Supplementary information** is available in the online version of the paper.

## **Acknowledgements**

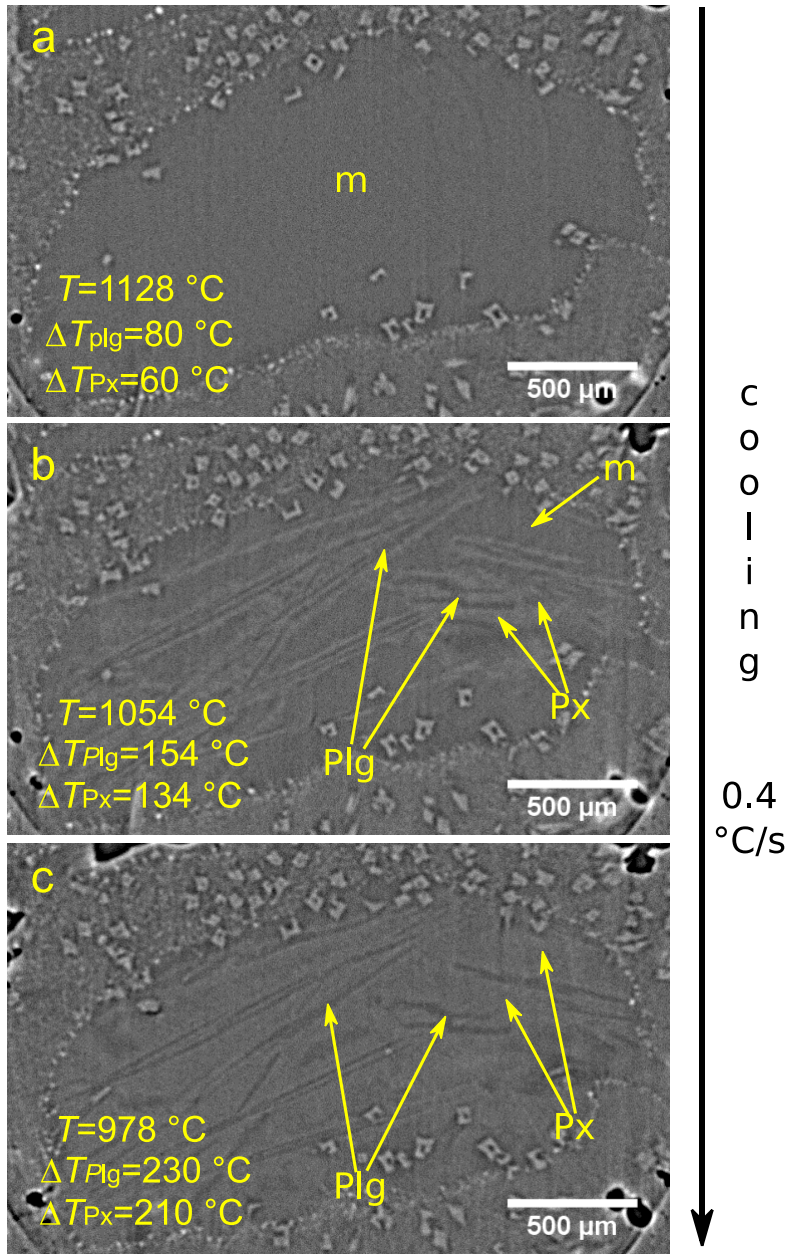
The research leading to these results has received funding from the RCUK NERC DisEqm project (NE/N018575/1) and (NE/M013561/1). The beamtime on I12 was provided by Diamond Light Source (EE16188-1) and laboratory space by the Research Complex at Harwell.

## **Author Contributions**

M.P., F.A., M.R.B., and P.D.L. conceived the research project. F.A., M.P., G.L.S., N.L.G., B.C., M.E.H., D.D.G., N.T.V., S.N., R.C.A., E.W.L., P.D.L. and M.R.B. contributed to the beamline experiments. F.A. collected the volcanic rocks for the starting material. D.D.G., H.M and R.A.B. prepared the starting material. F.A., M.P. and G.L.S performed image reconstruction. F.A. and M.P. performed image processing. F.A. performed image segmentation and analysis. G.L.S. performed simulations using the conduit model. R.A.B. and F.A. performed ex situ decompression experiments. E.C.B., F.A. and G.L.S. collected samples of the Etna 122 BC Plinian eruption. E.C.B. and F.A. acquired and analysed back-scattered electron images of Etna Plinian eruption's samples. F.A., G.L.S., M.R.B., M.P. and E.C.B. wrote the manuscript, with contributions from all other authors.

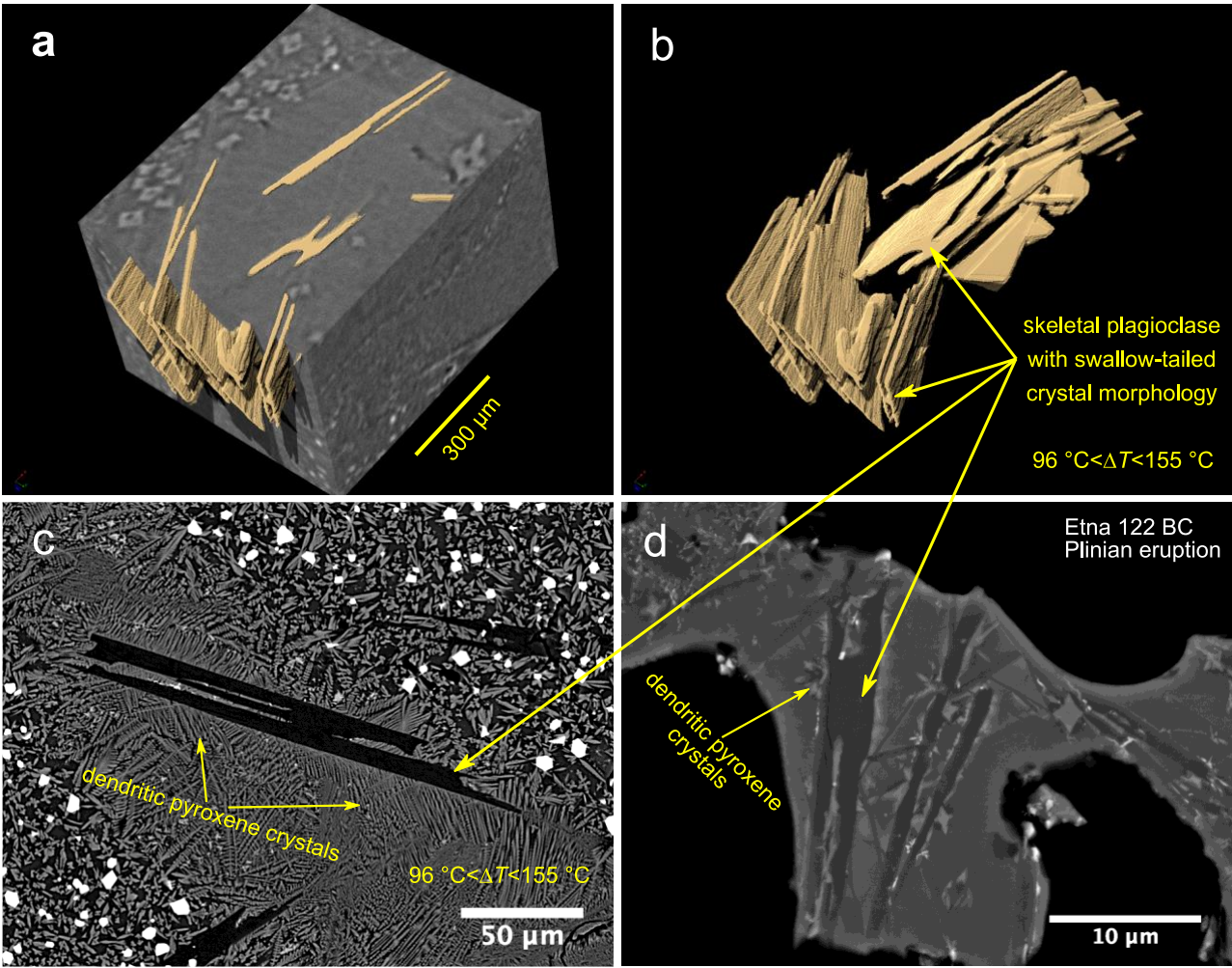
## **Author Information**

Reprints and permissions information is available at [www.nature.com/reprints](http://www.nature.com/reprints). The authors declare no competing financial interests. Readers are welcome to comment on the online version of the paper. Correspondence and requests for materials should be addressed to F.A. (fabio.arzilli@manchester.ac.uk)



637  
638 Figure 1. Crystallisation through time. Reconstructed axial slices during continuous cooling at  
639 0.4 °Cs<sup>-1</sup>: (a) frame after 24 s from the onset of the cooling, in which the temperature ranges  
640 between 1144 and 1112 °C (average 1128 °C); (b) frame after 208 s, in which the temperature  
641 ranges between 1073 and 1034 °C (average 1054 °C); (c) frame after 392 s, in which the  
642 temperature ranges between 997 and 959 °C (average 978 °C). m = melt; plg = plagioclase; px =  
643 pyroxene.

644

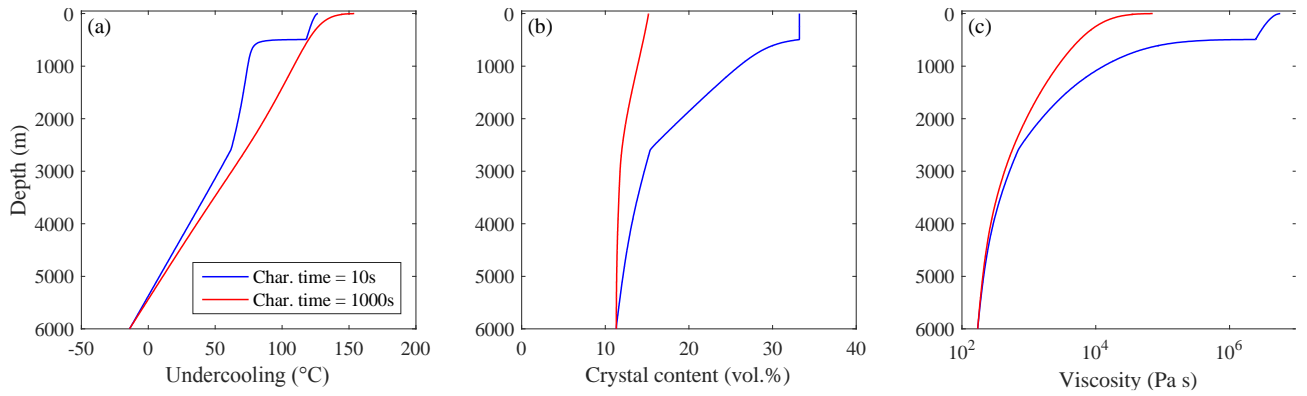


646

647

648 Figure 2. Plagioclase crystal morphology. (a) The 3D volume rendering of sample SS1150 shows  
649 the morphology and the spatial distribution of plagioclase crystals that formed during the rapid  
650 cooling at  $96 < \Delta T < 155$  °C. (b) 3D view of the plagioclase with swallow-tailed crystal morphology.  
651 (c) Back scattered electron image of plagioclase with swallow-tailed crystal morphology. (d) Back  
652 scattered electron image of plagioclase with swallow-tailed crystal morphology produced during the  
653 Etna 122 B.C Plinian eruption. Note heterogeneous nucleation of pyroxene around plagioclase, seen  
654 as a light-coloured halo, and similar to that seen in figure 1b.

655

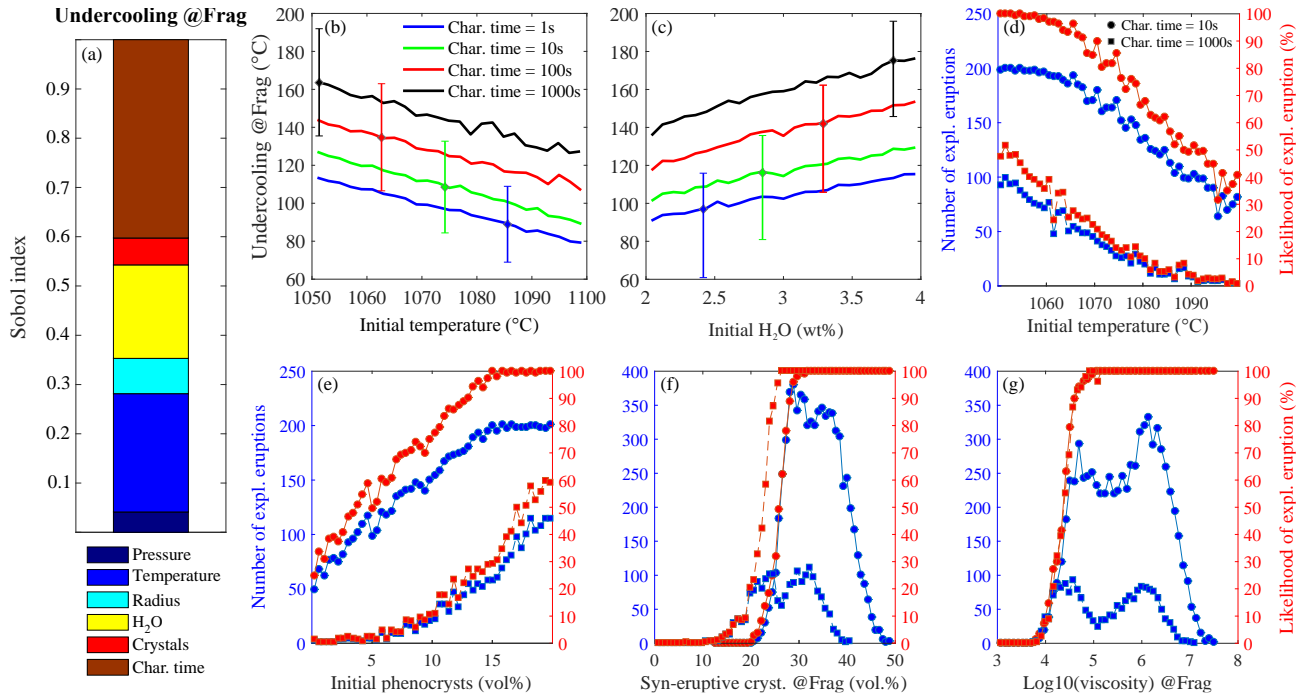


656

657

658 Figure 3. Model results during magma ascent. (a) Undercooling as a function of depth, calculated  
 659 for  $\tau(c) = 10$  (blue) and 1000 s (red). Cooling is driven by adiabatic expansion of gas, mitigated by  
 660 latent heat of crystallisation particularly in the fast crystallising case. (b) Crystal content in vol%,  
 661 demonstrating the rapid increase in crystal load when  $\tau(c) = 10$  s. (c) Magma viscosity,  
 662 demonstrating that the higher crystal load produces 3-4 order of magnitude increase in viscosity,  
 663 leading to fragmentation.

664



665

666

667

668

669

670

671

672

673

674

675

676

677

678

679

680

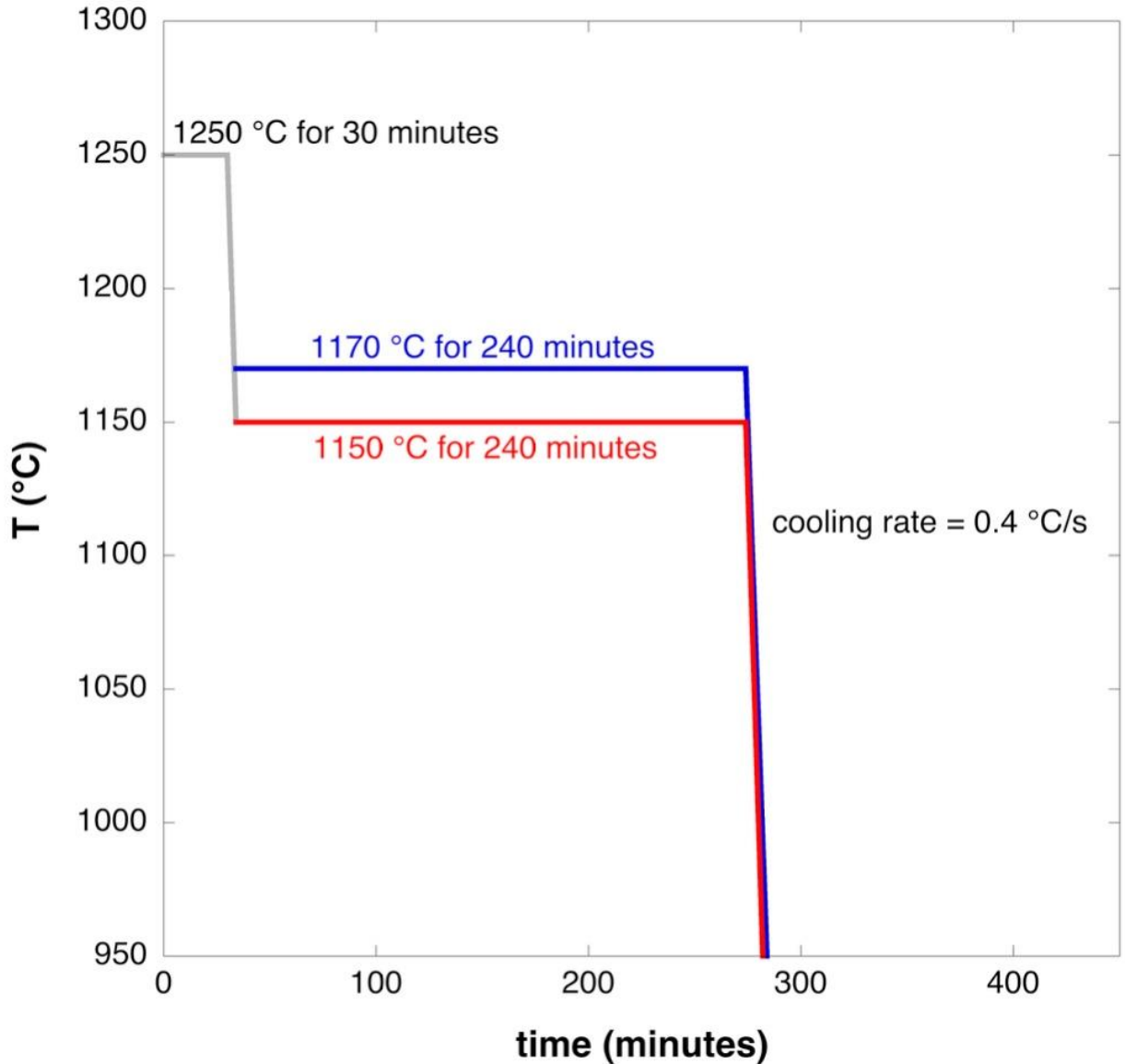
681

Figure 4. Relationships between characteristic time, initial temperature, initial H<sub>2</sub>O content of the magma, syn-eruptive crystal content and magma viscosity and the undercooling of the system at the fragmentation level. These figures were calculated using repeated runs of the model while changing individual parameters to reveal the sensitivity of the system to each parameter. Likelihood of explosive eruption as a function of a specific parameter arises from the ratio between the number of model runs producing explosive eruptions divided by the total number of model runs used to test that parameter. Therefore, this is not a probabilistic assessment of eruption risk, but instead depends on the critical model parameters, which control when fragmentation occurs, and the calculated probabilities depend on the choice of upper and lower limits chosen for each investigated parameter. (a) Sobol index. (b) Undercooling vs magma temperature before ascent. (c) Undercooling vs the initial H<sub>2</sub>O content of the magma (dissolved and exsolved). For a given input value, the solid lines are the mean of a given output parameter obtained from all the simulations assuming that input value. The error bars, instead, represent the spread of that output values with respect to the corresponding mean. (d) Frequency of explosive eruptions vs magma temperature before ascent. (e) Explosion frequency vs initial phenocryst content. (f) Frequency of explosive

682 eruptions vs syn-eruptive crystal content at the fragmentation level. (g) Frequency of explosive  
683 eruptions vs magma viscosity at the fragmentation level.  
684

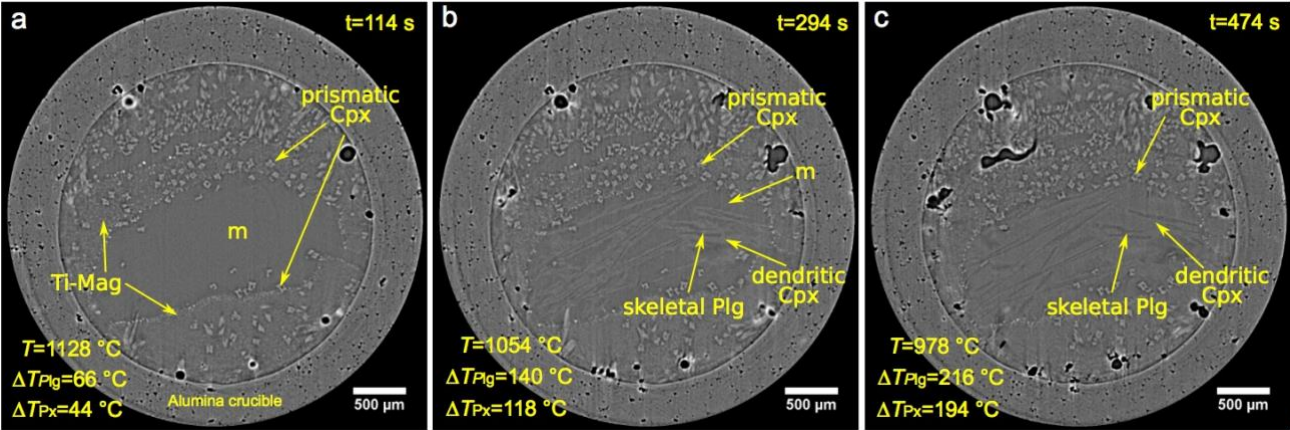


## Supplementary Information



**Supplementary Figure 1. Experimental conditions of *in situ* 4D experiments.** The glassy cylinders were heated *in situ* in the Alice furnace up to 1250 °C for 30 minutes. After the initial annealing period, crystallisation was induced by decreasing temperature from 1250 °C to 1170 °C (SS1170) or 1150 °C (SS1150) at ambient pressure, holding at the final temperature for 240 minutes. After this step, the temperature was perturbed by a rapid cooling at rate of 0.4 °C/s, reaching ~950 °C in ~8 minutes.

703



704

705

706

707

708

709

710

711

712

713

714

715

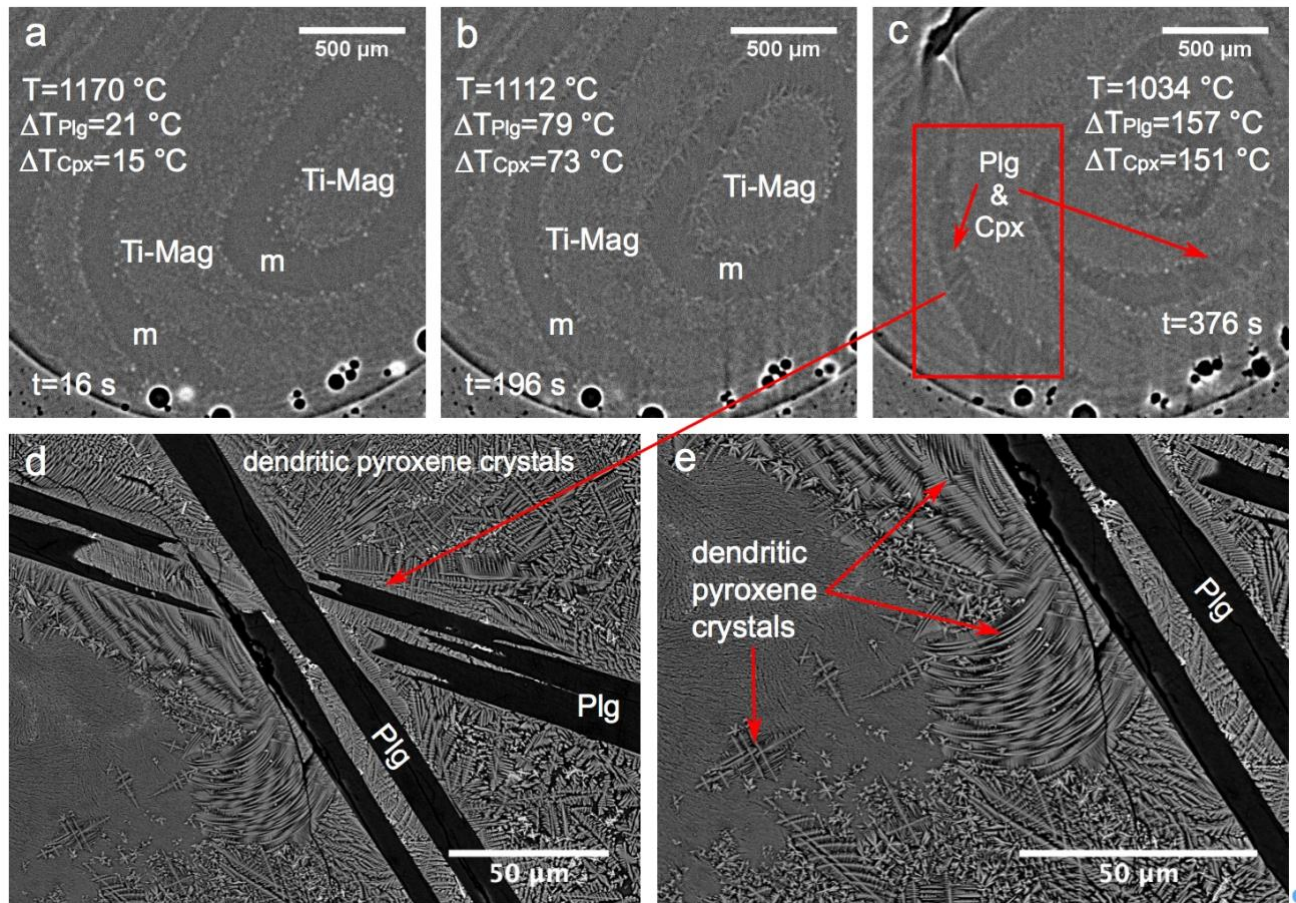
716

717

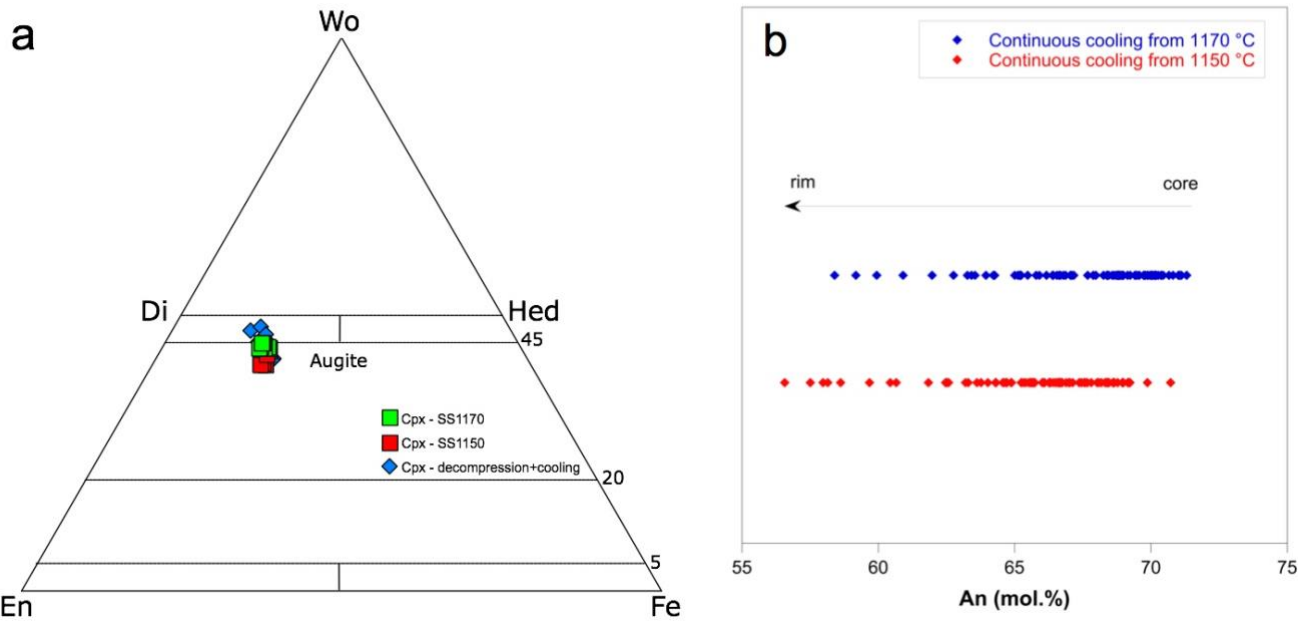
718

719

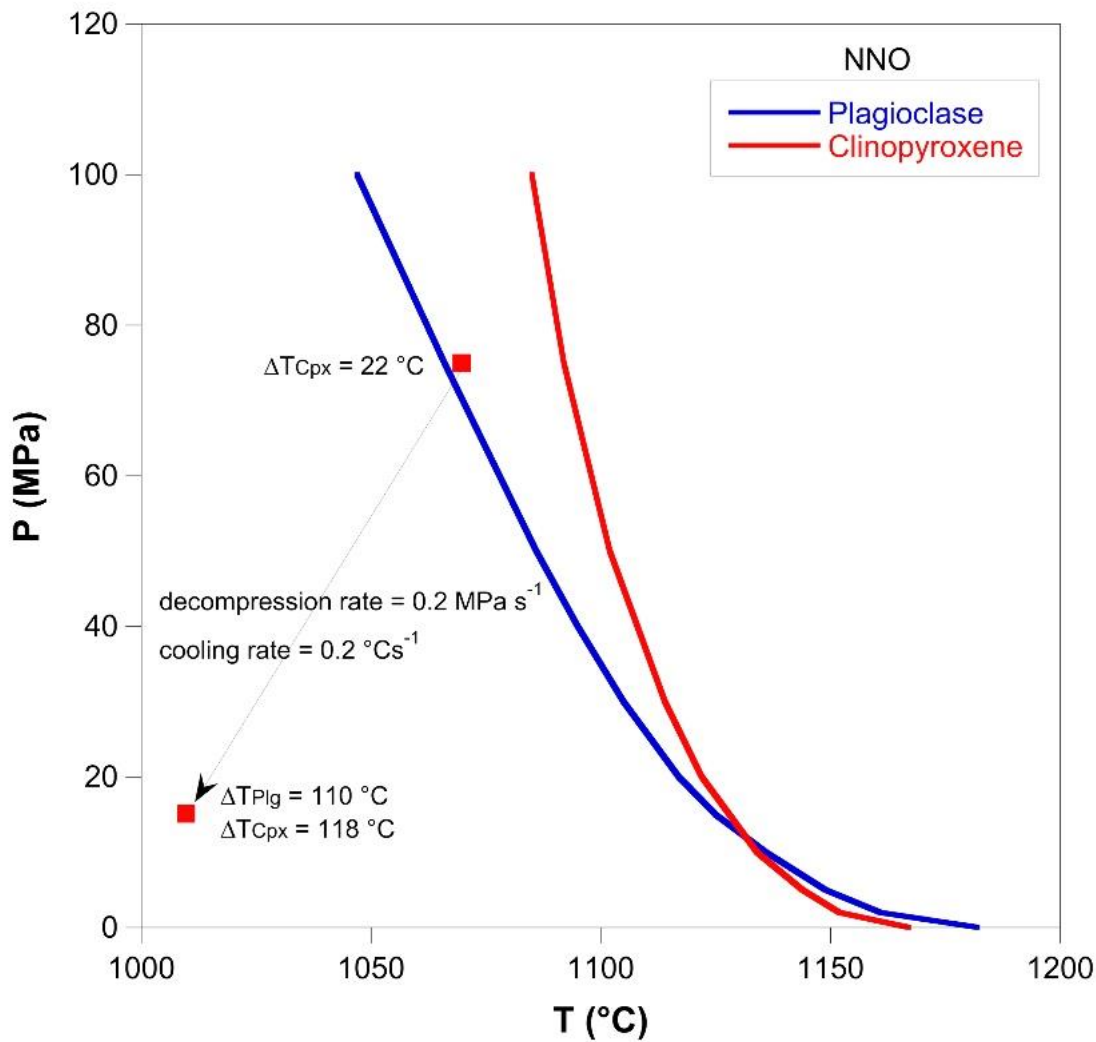
**Supplementary Figure 2. Crystallisation through time during experiment SS1150.** Reconstructed axial slices during continuous cooling at  $0.4\text{ }^{\circ}\text{C s}^{-1}$ : **a**, frame represents the texture after 114 s from the onset of the cooling in which the temperature ranges between 1144 and 1112  $^{\circ}\text{C}$  (average 1128  $^{\circ}\text{C}$ ); **b**, frame after 294 s, in which the temperature ranges between 1073 and 1034  $^{\circ}\text{C}$  (average 1054  $^{\circ}\text{C}$ ); **c**, frame after 474 s, in which the temperature ranges between 997 and 959  $^{\circ}\text{C}$  (average 978  $^{\circ}\text{C}$ ). m = melt; Plg = plagioclase; Cpx = clinopyroxene; Ti-Mag: titanomagnetite. The acquisition time of each frame is 90 s. t = time from the onset of the cooling to the end of the frame acquisition.



**Supplementary Figure 3. Crystallisation through time during experiment SS1170.** Reconstructed axial slices during continuous cooling at  $0.4\text{ }^{\circ}\text{C s}^{-1}$ : **a**, this frame shows the first 16 s from the onset of the cooling, in which the temperature ranges between 1170 and 1165  $^{\circ}\text{C}$ ; **b**, frame after 196 s, in which the temperature ranges between 1131 and 1092  $^{\circ}\text{C}$  (average 1112  $^{\circ}\text{C}$ ); **c**, frame after 376 s, in which the temperature ranges between 1053 and 1015  $^{\circ}\text{C}$  (average 1034  $^{\circ}\text{C}$ ). m = melt; Plg = plagioclase; Cpx = pyroxene; Ti-Mag: titanomagnetite. The acquisition time of each frame is 90 s. t = time from the onset of the cooling to the end of the frame acquisition.

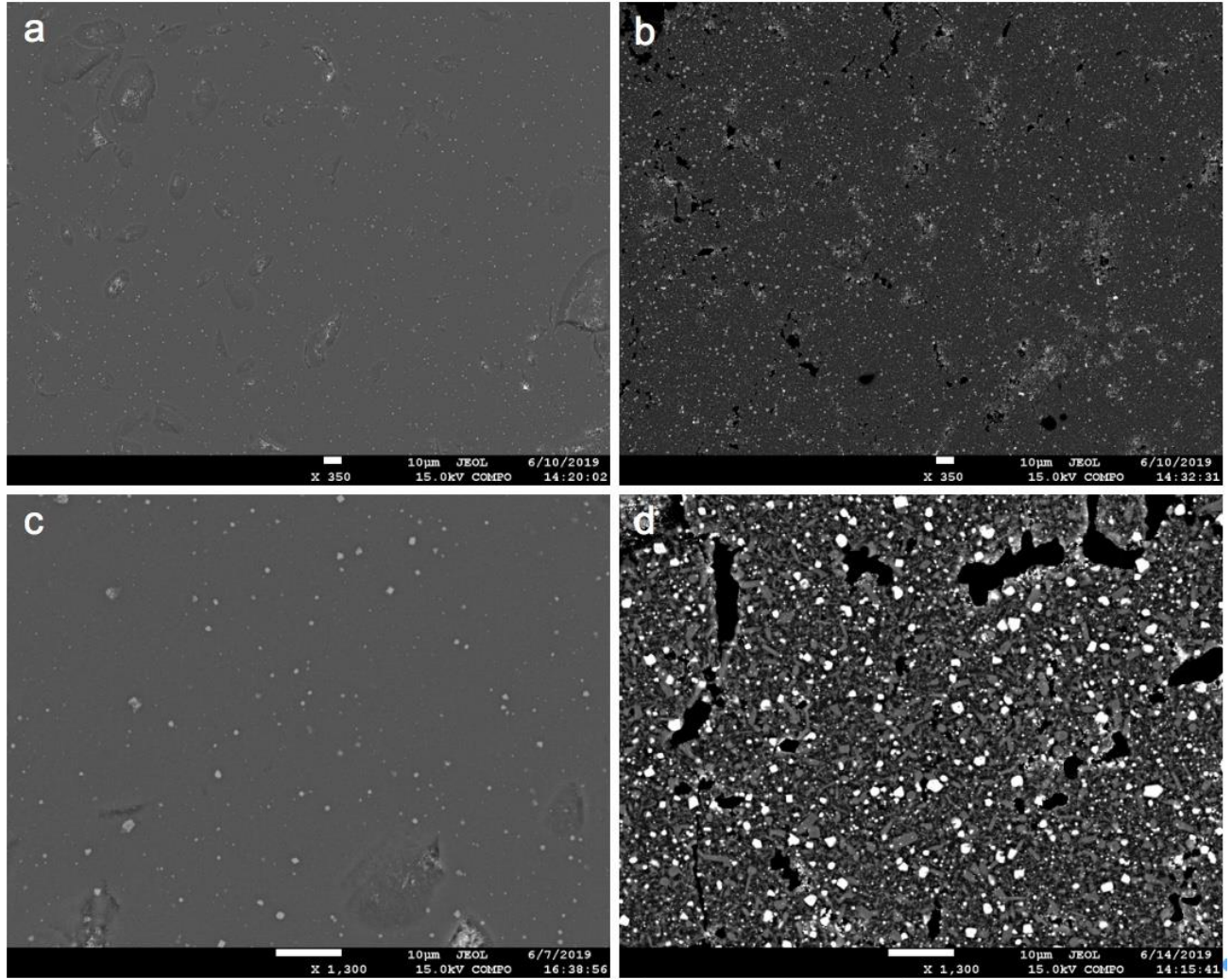


**Supplementary Figure 4. Chemical compositions of pyroxene and plagioclase formed during experiments.** **a**, Compositions of pyroxene crystals during rapid cooling at ambient pressure (SS1170 and SS1150) and rapid decompression and cooling (Etna\_7\_C): green square=SS1170; red square=SS1150; blue diamond=Etna\_7\_C. En: enstatite; Fs: ferrosilite; Di: diopside; Hd: hedenbergite; Wo: Wollastonite. **b**, Anorthite contents of plagioclase crystals formed during *in situ* experiments (SS1170 and SS1150).



**Supplementary Figure 5. *Ex situ* experimental conditions of rapid cooling and decompression experiment.** The experimental approach consisted of holding the sample for 30 minutes at 75 MPa and 1070 °C before being decompressed and cooled. The first experiment was quenched after 30 minutes at 75 MPa and 1070 °C, in order to texturally characterise the initial conditions before that fast decompression and cooling were applied. In the second experiment, after 30 minutes pressure and temperature were decreased continuously in 300 s at 0.2 MPa s<sup>-1</sup> and 0.2 °Cs<sup>-1</sup> respectively, reaching 15 MPa and 1010 °C. Final pressure was chosen as approximate fragmentation pressures calculated by modeling. Decompression and cooling rates were predicted from the conduit model used in this study. Plagioclase and clinopyroxene liquidus were obtained with Rhyolite-MELTS software (version 1.2), using the composition of our starting material.





**Supplementary Figure 6.** Textures of *ex situ* experiments. Back scattered images show the textures of: **a, c**, an hydrous basalt quenched at 75 MPa and 1070 °C after 30 minutes (sample Etna7\_C) and **b, d**, an hydrous basalt quenched after a rapid decompression and cooling at 15 MPa and 1010 °C (sample Etna7\_B). **a, c**, The texture of sample Etna7\_C is characterised by oxide crystals and glassy matrix. **b, d**, The mineral assemblage of sample Etna7\_B consists of oxide, clinopyroxene and plagioclase. Oxide formed mostly at initial conditions, after 30 minutes at 1070 °C and 75 MPa (see Etna7\_C, panels **a** and **c**). The rapid decompression and cooling allowed the achievement of large  $\Delta T$ s (>100 °C; see Supplementary Fig. 6) in 300 s, favouring predominantly clinopyroxene crystallisation, plagioclase and oxide. This indicates that  $\tau^{(c)}$  is 60 s, in agreement with the order of magnitude estimated from *in situ* experiments.

789 **Supplementary Table 1.** Chemical composition of the starting material.  
790

Oxide (wt.%)	Bulk composition	st. dev.	Residual melt after 4h at 1170 °C	Residual melt after 4h at 1150 °C
SiO <sub>2</sub>	48.41	0.16	52.18	52.99
TiO <sub>2</sub>	1.79	0.07	1.7	1.69
Al <sub>2</sub> O <sub>3</sub>	16.22	0.50	16.86	17.5
FeO*	10.66	0.30	6.05	5.4
MnO	0.20	0.03	0.22	0.24
MgO	6.20	0.32	5.34	4.77
CaO	10.66	0.19	11.23	10.54
Na <sub>2</sub> O	3.41	0.20	3.74	3.99
K <sub>2</sub> O	1.90	0.07	2.09	2.24
P <sub>2</sub> O <sub>5</sub>	0.54	0.04	0.59	0.64
Total	99.85		100	100

791 note: FeO\* = total iron as FeO. The residual melt compositions after the 240 minutes have been obtained with a mass  
792 balance calculation, which indicates that they are basaltic trachyandesite. We considered that the main difference  
793 between experiment SS1150 and SS1170 is that the abundance of pyroxene after 4 hours at 1150 °C is higher than that  
794 at 1170 °C. Experiment SS1170 (after 4 hour at 1170 °C) indicates that prismatic pyroxene crystals are ~ 1 vol.% and  
795 oxide crystals are ~8 vol. %, whereas in the experiment SS1150 (after 4 hour at 1150 °C) prismatic pyroxene crystals  
796 are more abundant (~8 vol.%).

797  
798  
799  
800  
801  
802 **Supplementary Table 2.** Results of plagioclase and pyroxene growth rates during continuous  
803 cooling at 0.4 °C/s.  
804

3D analysis							
<i>Plagioclase crystal growth rate</i>							
Sample	Growth duration (s)	L3Dmax (cm)	YL3Dmax (cm s <sup>-1</sup> )	L3Dmin (cm)	YL3Dmin (cm s <sup>-1</sup> )	L3Dave (cm)	YL3Dave (cm s <sup>-1</sup> )
SS1150	90	2.77E-02	1.54E-04	6.35E-03	3.53E-05	1.39E-02	7.74E-05
2D analysis							
<i>Plagioclase crystal growth rate</i>							
Sample	Growth duration (s)	Lmax (cm)	YLmax (cm s <sup>-1</sup> )	Lmin (cm)	YLmin (cm s <sup>-1</sup> )	Lave (cm)	YLave (cm s <sup>-1</sup> )
SS1170	180	2.73E-02	7.59E-05	1.15E-02	3.20E-05	1.78E-02	4.96E-05
<i>Pyroxene crystal growth rate</i>							
Sample	Growth duration (s)	Lmax (cm)	YLmax (cm s <sup>-1</sup> )				
SS1170	180	3.6E-03	2.0E-05				
SS1150	180	3.24E-03	1.80E-05				

805 note: L3Dmax = average length of the 15 largest crystals measured in the 3D domain; YL3Dmax = growth rate  
806 calculated using the 15 largest crystals; L3Dmin = average length of the 15 smallest crystals measured in the 3D  
807 domain; YL3Dmin = growth rate calculated using the 15 smallest crystals; YL3Dave = the average value of growth rate  
808 obtained taking into account the length all the crystals analysed; Lmax = average length of the 15 largest crystals  
809 measured in the 2D domain; YLmax = growth rate calculated using the 15 largest crystals.

810  
811

812 **Supplementary Table 3.** Experimental conditions for ex situ experiments performed with TZM  
 813 cold seal pressure vessel apparatus.

814

Sample	Ti (°C)	Pi (Mpa)	ti (s)	decompression rate (Mpa s-1)	cooling rate (°Cs-1)	Tf	Pf
Etna7_C	1070	75	1800	-	-	1070	75
Etna7_B	1070	75	1800	0.2	0.2	1010	15

815  
 816  
 817  
 818  
 819  
 820 **Supplementary Table 4.** Summary of X-ray microtomography acquisition conditions and image  
 821 processing details of the volumes of interest (VOI) for experiment ET1150.

822  
 823

Energy	Distance sample to detector	Projection	Exposure time	Voxel size	Original imaged volume	Analysed VOI	Segmentation
keV	mm	number	s	µm³	pixels (mm³)	mm³	
53	2300	1800	0.05	3.2x3.2x3.2	1683x1683x1383 (128.4)	8.2037	semi-automatic volume segmentation Avizo software v. 8.0

824  
 825  
 826  
 827  
 828  
 829